Revisiting the role of *Toxoplasma gondii* ERK7 in the maintenance and stability of the apical complex

Nicolas Dos Santos Pacheco[1*], Nicolò Tosetti[1*], Aarti Krishnan[1], Romuald Haase[1] & Dominique Soldati-Favre[1#]

[1]Department of Microbiology and Molecular Medicine, Faculty of Medicine, University of Geneva. 1 Rue Michel-Servet, 1211 Geneva, Switzerland

Running title: *Revisiting the role of ERK7 in Toxoplasma gondii*

*These authors contributed equally to this work

#Address correspondence to Dominique Soldati-Favre: Dominique.Soldati-Favre@unige.ch

Abbreviations: apical cap protein AC; subpellicular microtubules, SPMTs; inner membrane complex, IMC; Extracellular signal-regulated kinase 7, ERK7.

Keywords: Apicomplexa, *Toxoplasma gondii*, conoid, apical cap, subpellicular microtubules, comparative proteomics, egress, motility, invasion, microneme secretion.

Abstract

Toxoplasma gondii ERK7 is known to contribute to the integrity of the apical complex and to be involved only in the final step of the conoid biogenesis. In the absence of ERK7, mature parasites lose their conoid complex and are unable to glide, invade or egress from host cells. In contrast to a previous report, we show here that depletion of ERK7 phenocopies the depletion of the apical cap proteins AC9 or AC10. The absence of ERK7 leads to the loss of the apical polar ring, the disorganization of the basket of subpellicular microtubules and an impairment in micronemes secretion. Ultra-expansion microscopy (U-ExM) coupled to NHS-Ester staining on intracellular parasites offers an unprecedented level of resolution and highlights the disorganization of the rhoptries as well as the dilated plasma membrane at the apical pole in the absence of ERK7. Comparative proteomics analysis of wild-type and ERK7 or AC9 depleted parasites led to the disappearance of known, predicted, as well as putative novel components of the apical complex. In contrast, the absence of ERK7 led to an accumulation of microneme proteins, resulting from the defect in exocytosis of the organelles.

Importance

The conoid is an enigmatic, dynamic organelle positioned at the apical tip of the coccidian subgroup of the Apicomplexa, close to the apical polar ring (APR) from which the subpellicular microtubules (SPTMs) emerge and at the site of microneme and rhoptry secretory organelles exocytosis. In *Toxoplasma gondii,* the conoid protrudes concomitantly to microneme secretion, during egress, motility and invasion. The conditional depletion of the apical cap structural protein AC9 or AC10 leads to a disorganization of SPTMs as well as the loss of APR and conoid that result in microneme secretion defect and block in motility, invasion and egress. We show here that depletion of the kinase ERK7 phenocopies completely AC9 and AC10 mutants. Moreover, the combination of ultrastructure expansion microscopy with an NHS ester staining revealed that ERK7 depleted parasites exhibit a dilated apical plasma membrane and a mis-positioning of the rhoptry organelles.

Introduction

The Apicomplexa phylum is defined by the so-called apical complex, a structure that harbors unique secretory organelles, termed rhoptries and micronemes, as well as membranous and cytoskeletal elements that critically contributes to parasite dissemination. The overall cytoskeleton is made of three interacting layers, conferring structure and stability to the parasite: the inner membrane complex (IMC), formed by a patchwork of flattened vesicles, the subpellicular network (SPN) composed of intermediate filaments-like proteins termed alveolins and the subpellicular microtubules (SPMTs). The most apical region of the IMC, called the apical cap, is formed by a single vesicle and was shown to participate to the apical complex stability (Back et al. 2020; O'Shaughnessy et al. 2020; Tosetti et al. 2020) Members of the coccidian subgroup possess an additional open-barrel shaped structure made of unique fibers of tubulin polymers termed the conoid (Hu et al. 2002), with two pre-conoidal rings (PCRs) at the top and two short intra-conoidal microtubules on the inside (Dos Santos Pacheco et al. 2020). The conoid lays between the apical polar ring (APR) which serves as microtubule organizing center (MTOC) for the spiraling SPMTs. The apical cap proteins 9 and 10 (AC9, AC10) were previously shown to be SPN resident proteins whose depletion resulted in the loss of the conoid and the APR, and disorganization of the SPMTs at the apical pole (Back *et al.* 2020; Tosetti *et al.* 2020). The conoid is the site of convergence for calcium and lipid-mediated signaling cascades that coordinate microneme secretion and actin polymerization, and is also the site of for the glideosome, the molecular machinery powering parasite gliding motility (Bisio & Soldati-Favre 2019). Strikingly AC9 and AC10 depleted parasites were severely impaired in microneme secretion and consequently unable to move, invade or egress from host cells. We postulated that the loss of the conoid and SPMTs disorganization, could result from the disappearance of the APR. Concordantly another study reported that the double knock-out of two APR proteins (APR1 and KinA) led to the fragmentation of the APR, partial detachment of the conoid and reduced microneme exocytosis (Leung et al. 2017). In contrast, depletion of the mitogen-activated protein kinase (MAPK) ERK7 reportedly cause the loss of conoid in mature

parasite without seemingly affecting microneme secretion nor APR integrity (O'Shaughnessy *et al.* 2020). Moreover, AC9 was assigned a dual role in localizing ERK7 at the apical cap and in regulating its kinase activity and substrate specificity (Back *et al.* 2020). Another protein, the conoidal ankyrin repeat-containing protein (CPH1) was also reported to contribute to the conoid integrity in extracellular parasites. CPH1 depleted parasites harbored shortened, partially collapsed conoids, again without seemingly impacting on microneme secretion (Long et al. 2017a).

Here, we have revisited the role of ERK7 and CPH1 in microneme secretion. Depletion of ERK7 phenocopies strictly the depletion AC9 or AC10, leading not only to the loss of the conoid but also the disappearance of the APR and a severe impairment in induced microneme secretion. A comparative proteomics analysis of wild-type and ERK7 or AC9 depleted parasites highlighted the loss of known, as well as novel candidate proteins composing the apical complex. Conversely the accumulation of microneme proteins reflected the severe defect in exocytosis of these secretory organelles.

Results

ERK7 is essential for the stability of the conoid complex and the organization of the subpellicular microtubules in mature parasites

Three mitogen-activated protein kinases (MAPKs) are encoded in the genome of *T. gondii* and conserved across the superphylum of the Alveolata, except for TgMAPK-like 1 which is missing in haemosporidia and piroplasmida orders (Lacey et al. 2007; Talevich et al. 2011); their respective localization and function in *T. gondii* and *Plasmodium* spp. are summarized in Figure S1A. Briefly, TgMAPK-like 1 and TgMAPK2 are both involved in different steps of parasite replication (Suvorova et al. 2015; Hu et al. 2020), while TgERK7 is involved in conoid biogenesis thus hampering parasites invasion, egress and dissemination (O'Shaughnessy *et al.* 2020). The *Plasmodium* spp. orthologues of TgERK7 (Pf/PbMAP-1) and TgMAPK2 (PF/PbMAP-2) are

103 dispensable in the asexual blood stage with only Pf/PbMAP-2 required for male gametogenesis
104 (Khan et al. 2005; Rangarajan et al. 2005; Tewari et al. 2005; Hitz et al. 2020).
105 TgERK7 was carboxy-terminally tagged with the mAID-HA (ERK7-mAID-HA) at the endogenous
106 locus and shown to be tightly downregulated upon addition of auxin (IAA) (Figure S1B) and
107 localized at the apical cap of both mature and daughter cells (Figure S1C). As previously reported,
108 parasites depleted in ERK7 fail to form lysis plaques in a monolayer of human foreskin fibroblasts
109 (HFFs) after 7 days of IAA treatment (Figure S1D). Given the close relationship reported between
110 AC9 and ERK7, the cytoskeletal integrity was checked by deoxycholate (DOC) extraction. As
111 observed in absence of AC9 or AC10, the cytoskeleton of parasites depleted in ERK7 is
112 disassembled (Figure 1A). In addition to the loss of conoid, the APR has disappeared, leading to a
113 wide apical opening, explaining the detached SPMTs visible by DOC extraction (Figure 1B).
114 Ultrastructure expansion microscopy (U-ExM) was applied here for the first time on intracellular
115 parasites to compare with observations made on extracellular parasites, using the ERK7-mAID-HA
116 strain further modified by Ty-epitope tagging of AC2, a marker of the alveolin network (ERK7-
117 mAID-HA / AC2-Ty). As previously shown with AC9 deleted parasites, the absence of ERK7 led
118 to the loss of both conoid and APR in mature parasites, while the nascent daughter cells still
119 possessed an intact apical complex (Figure 1C). Overall AC2 was not dramatically affected by
120 ERK7 depletion; however, occasionally, AC2 was either not present apically or was markedly
121 reduced in some parasites (Figure 1C). The same observation was made with another apical cap
122 protein, ISP1 (Figure S1E).
123
124 **The apical polar ring is lost in mature ERK7 depleted parasites**
125 To further confirm the loss of the APR, three APR markers were epitope tagged in the ERK7-
126 mAID-HA strain, namely RNG1, APR1 and KinA (Tran et al. 2010; Leung *et al.* 2017). RNG1, a
127 very late maker of parasite division, was not visible at the APR of mature parasites (Figure 2A and
128 2B; Figure S2A); whereas the protein was still detectable by western blot analysis (Figure 2A).

129 Remarkably, the remaining RNG1 signal is mis-localized in the absence of ERK7, accumulating
130 mainly at the posterior pole of the parasites (Figure 2A; Figure S2A). The two other APR markers
131 were lost exclusively in the mature parasite but present in nascent daughter cells, confirming ERK7
132 role occurring late in parasite division (Figure 2C and 2D). In contrast to RNG1, APR1 and KinA
133 are both degraded based on western blot analysis (Figure 2C and 2D).
134

135 **Rhoptries are disorganized in mature ERK7 depleted parasites by NHS-Ester staining**
136 **coupled to U-ExM**

137 Next, to gain further insight into the morphology of the ERK7 depleted parasites, we coupled U-
138 ExM newly adapted to *T. gondii* (Tosetti *et al.* 2020) with the fluorescent dye N-
139 hydroxysuccinimide ester (NHS-Ester) able to bind to primary amines on proteins. Remarkably, this
140 combination allows the observation of a wide range of anatomical features while approaching the
141 resolution of electron microscopy (EM) (M'Saad & Bewersdorf 2020). This technique allowed the
142 visualization a wide spectrum of recognizable ultrastructures (movie 1 and 2) with a non-exhaustive
143 list of such features presented in individual stacks (Figure S3). As expected, in ERK7 depleted
144 parasites the conoid was clearly absent from mature parasites while still present in forming daughter
145 cells (Figure 3A, movie 3 and 4). Strikingly the neck of the rhoptries also detected with anti-RON9
146 antibodies, are still apical but dispersed compared to their apical positioning in presence of ERK7.
147 Interestingly, the so-called "neck" of the rhoptries seems to not extend all the way up to the conoid.
148 This observation was also confirmed with an anti-RON4 antibody (data not shown). Furthermore
149 as previously observed by EM for AC9 depleted parasites (Tosetti *et al.* 2020), in the absence of
150 ERK7 the plasma membrane was dilated at the apical pole (Figure 3A).
151

152 **ERK7 depleted parasites are defective in induced microneme secretion**

153 The dilated plasma membrane was examined by staining for the major surface antigen (SAG1) and
154 both in AC9 and ERK7 depleted conditions, the integrity of the membrane appeared compromised

155 in some intracellular parasites (Figure 4A). This leads to an apparent releases of few micronemes
156 outside the parasite body (Figure 4B; Figure S4A and S4B), as previously reported by EM in the
157 absence of AC9 (Tosetti *et al.* 2020).
158 Although AC9 and ERK7 are both essential for parasite survival, depleted mutants are not affected
159 in intracellular growth and replication (Figure 4C). In contrast, both mutants are seemingly able to
160 lyse the parasitophorous vacuole membrane (PVM) but remained trapped inside the host cell even
161 after the host cell detached in floating "bubbles" suggesting at least a partial microneme secretion
162 defect (Figure 4C). While depletion of ERK7 was reported not to impact on microneme secretion, a
163 severe exocytosis defect was observed in absence of AC9 (Back *et al.* 2020; O'Shaughnessy *et al.*
164 2020; Tosetti *et al.* 2020). The microneme secretion used by O'Shaughnessy *et al,* was based on a
165 luciferase assay applied previously to CPH1-mAID (Long et al. 2017). Here the induced secretion
166 assay was monitored by detection of cleaved released MIC2 in the supernatant and quantified by
167 western blot. Under these conditions, ERK7-mAID-HA treated with IAA showed a complete block
168 in microneme secretion as reported for AC9 (Figure 4D). As control, the CPH1-mAID strain was
169 generated (Figure S4C and S4D) and shown to exhibit a milder defect in microneme secretion
170 indicating that the discrepancy can be explained only in part by the type of assay used (Figure S4E).
171

172 **Comparative proteomics of wild-type and ERK7/AC9 depleted parasites identifies novel**
173 **candidate components of the apical complex**

174 Given the dramatic disappearance of the structure as well as the protein markers of the conoid and
175 APR in both AC9 and ERK7 depleted parasites, we performed a comparative proteomic analysis by
176 mass spectrometry to gain further knowledge about the composition of the apical complex. The
177 datasets analysis revealed a good overall coverage in comparison to the hyperLOPIT dataset
178 (3,832 *T. gondii* detected proteins) (Barylyuk et al. 2020), with a total of 3477 and 3483 proteins
179 detected in ERK7 and AC9 samples, respectively (Figure 5C). In agreement with previously
180 published data and proteomics datasets, numerous known apical complex proteins disappeared in

both AC9 and ERK7 depleted parasites (Figure 5A, 5B, 5D and Figure 6A). Out of the 17 most significantly depleted proteins in both datasets, 14 were already localized at the apical pole of the parasite (Figure 6A). Overall, the analysis points toward at least a dozen of plausible novel candidate proteins potentially associated to the apical complex.

Comparative proteomics of wild-type and ERK7 and AC9 depleted parasites show an accumulation of microneme proteins and components of the IMC

Beside the loss of components of apical complex and conversely, other distinct sets of proteins accumulate in ERK7 and AC9 depleted parasites, respectively (Figure 5A, 5B, 5D and Figure 6B). In the absence of ERK7, known microneme proteins as well as proteins predicted by hyperLOPIT (Barylyuk et al. 2020) to be associated with micronemes are significantly more abundant. This is easily accounted for by the severe microneme exocytosis defect observed in the mutant parasites. In AC9 depleted parasites, microneme proteins also accumulated however other proteins predicted to be localized at the IMC or dense granules are overrepresented. Out of the 17 proteins enriched in both datasets and not localized experimentally to date, 7 share a cell cycle transcription profile common to known IMC proteins (Figure 6B and Figure S5). A comprehensive list of the comparative proteomics analysis of ERK7 and AC9 mutants is presented in Dataset 1.

Discussion

AC9 is a component of the alveolin network proposed to serve as regulatory platform for ERK7 kinase activity (Back *et al.* 2020). In this study we have revisited the role of ERK7 in the integrity of the apical complex of *T. gondii* in light of unmatching phenotypic consequences compared to AC9 depletion (O'Shaughnessy *et al.* 2020; Tosetti *et al.* 2020). ERK7 depleted parasites phenocopied AC9 and AC10 depletion except that APR was shown to be still present and microneme secretion was not affected. Here a new ERK7-mAID-HA strain was generated and confirmed to be severely affected in invasion and egress from infected cells. U-ExM analysis

proved that like AC9 and AC10, ERK7 is required to maintain the conoid stability but also to preserve the tethering of the SPMTs in mature parasites. In contrast to the previous report, the depletion of ERK7 leads the disappearance of the APR with the degradation of APR1 and KinA and the mislocalization of RNG1. As a late marker of the APR, RNG1 might not be a structural component *per se* of the APR but rather associated to the structure only in mature parasites. The absence of the APR might explain why this protein end up in the residual body in ERK7 depleted parasites. The absence of APR also explains the wide apical opening observed in U-ExM and why detached individual microtubules are observed in deoxycholate extraction experiments. The APR is likely lost upon parasite final maturation as it presumably serves as MTOC for the SPMTs.

The NHS-Ester staining coupled with U-ExM offers novel opportunities to study in detail the internal structures of the parasite in its vacuolar niche. For example, in the less well-studied parasites like *Cryptosporidium spp*. in which a very sparse number of antibodies have been raised for localization studies (Wilke et al. 2018). The NHS-Ester could be a staining of great value as it can virtually reveal all structures within the cell. Also, as shown in this study, some structures are very well stained with this method. The "ring structures" systematically observed presumably corresponds to the micropore or the ring structures described with GAPM2 and GAPM3, two resident proteins of the IMC (Nichols et al. 1994; Harding et al. 2019). The basal complex of the parasite appears extremely dense with this technique, probably highlighting a density of protein complexes present at the basal pole of the parasite. In addition, very small structures in dividing parasites like the centrocone and centromeres are surprisingly evident with the NHS-Ester staining while only EM could achieve such level of details (Francia et al. 2020). Further improvements of these methods could potentially help retaining membrane or lipid-bound epitope as well as reaching greater expansion ratio without the need of heavy instruments (Damstra et al. 2021).

The induced microneme secretion monitored here by excretory-secretory antigen detection via western blot provides radically opposing outcome for ERK7-mAID-HA compared to the published results based on the luciferase assay. The presence of the conoid seems absolutely required for

microneme secretion as no processed MIC2 can be detected in supernatant from parasites depleted in ERK7, AC9 or AC10 (Tosetti *et al.* 2020). Since O'Shaughnessy *et al*, used a very sensitive assay based on MIC2 fused to luciferase reporter we also generated a CPH1-mAID mutant previously analyzed by the same method to include in the analysis (Long *et al.* 2017a). The two assays are rather concordant for CPH1 depleted parasites although a mild defect in microneme secretion was not detected in the luciferase-based assay (Long et al. 2017). The accumulation of further processing of MIC2, only visible by western blot-based assay, reflects a defect in gliding motility due to the lack of posterior translocation of MIC2, and hence the over-representation of MIC2 protein trimmed by the apical subtilisin-like serin protease SUB1 (Lagal et al. 2010). It is plausible that the luciferase assay is too sensitive for the detection of minor defects microneme exocytosis, yet ERK7 depleted parasites have a very strong defect. Given that a fraction of these mutants was shown to exhibit a dilated apical plasma membrane, they might be more prone to lysis and could perturb the assay if parasites are not carefully washed before the experiment. In a conceptually distinct assay, O'Shaughnessy et al, also assessed microneme secretion by monitoring mVenus diffusion from the PV to the host cell cytoplasm. This diffusion is indicative of a permeabilization of the PVM by the action of the secreted microneme protein perforin PLP1 (Kafsack et al. 2009). AC9 and ERK7 depleted parasites are indeed able to lyse the PVM but remained trapped inside the host cell suggesting that a low level of microneme exocytosis was occurring in a few intracellular parasites but not sufficient to trigger complete egress and hence resulted in parasites trapped in floating detached host cells. Alternatively the discrepancies observed in ERK7 mutant with regard to the disappearance of the APR and ability to secrete microneme could be explained by revertant parasites that fail to respond anymore to IAA as mentioned by the authors (O'Shaughnessy *et al.* 2020).

Capitalizing on the loss of APR and conoid that resulted in degradation of several apical complex protein in both ERK7/AC9 depleted strains, we embarked on a proteomics analysis to compare the mutants to wild-type parasites and identify novel components of the affected structures. The

comparative analysis between each replicate revealed a striking quantitative reproducibility for the vast majority of proteins. Consequently, the subsets of proteins disappearing or accumulating in the samples emerged very clearly. A large set of proteins already known or predicted to be associated with the apical complex were detected while only a small number of potential new apical complex proteins were found, potentially reflecting some technical limitation of mass spectrometry in detecting small, low abundant or not easily digested proteins. Alternatively, the combination of approaches used so far to determine the repertoire of apical complex protein might be almost comprehensive.

Of relevance, known, as well as predicted microneme proteins are accumulating in ERK7 and AC9 deleted parasites, concordantly with their impairment in microneme exocytosis. This tendency was more prominent in the ERK7 depleted parasites since twice as many proteins were found significantly enriched in those parasites compared to the AC9 depleted ones (88 versus 41). This might be due to the intrinsic nature and role of the two proteins: while AC9 is a structural component of the alveolin network, ERK7 is an active kinase (Back *et al.* 2020). Some proteins enriched in the absence of ERK7 could be affected by the absence of kinase activity and not only be a consequence of the loss APR and conoid and the disassembly of SPMTs. In the absence of ERK7 or AC9, some proteins predicted by hyperLOPIT to localize at the dense granules, ER, Golgi, nucleus also accumulate (Barylyuk *et al.* 2020). The experimental assessment of their localization will be instrumental as some protein such as the product of TGGT1_254870, mainly predicted to localize at the nucleus was previously localized at the apical pole of the parasite (Long *et al.* 2017). Similarly, the product of TGGT1_243200, predicted to localize to the dense granules is associated to the IMC of nascent daughter cells (Chen *et al.* 2016).

Overall, with novel technologies such as U-ExM, NHS-Ester staining and comparative proteomics mass-spectrometry, a deeper look into the role of ERK7 was taken in this study. Our observations revealed that the loss of ERK7, a kinase likely phosphorylating several components (known and unknown) of the apical complex, indeed dislocates the conoid complex. The severe microneme

285 secretion defect also strengthens previous observations that exocytosis of these organelles, and as a
286 consequence, proper egress, gliding, motility and invasion of intracellular parasites, might not be
287 achieved without the presence of a structurally intact conoid.

288

289 **Figure legends**

290

291 **Figure 1 - ERK7 depletion caused major cytoskeletal defects at the apical pole**

292 **(A)** Extracellular parasites were extracted with deoxycholate (DOC) and placed on gelatin
293 coverslips. Depletion of ERK7 caused the collapse of the microtubular cytoskeleton as only single
294 microtubules can be visualized by IFA with α-tubulin antibody suggesting that the APR is no more
295 present in those mutants. **(B)** Ultrastructure expansion microscopy (U-ExM) highlighted the
296 absence of the APR and consequently an enlargement of the apical pole in ERK7 depleted parasites.
297 **(C)** U-ExM was applied in intracellular conditions with AC2 tagged in the ERK7 inducible strain.
298 Upon addition of IAA, the APR and conoid are missing exclusively in the mother cell and in some
299 severe cases of SPMTs disorganization the AC2 staining disappears from the apical cap too
300 (arrowhead). Scale bars = 2 mm.

301 **Figure 2 - Loss of apical markers in ERK7 depleted parasites**

302 **(A)** RNG1, a late marker of parasite division, failed to be incorporated in most of the parasites. APR
303 and RNG1 signals could be detected in parasite cytoplasm/residual body (asterisk). Western blot
304 analysis confirmed that RNG1 is not degraded. **(B)** Quantification of apical RNG1 in ERK7
305 depleted parasites. **(C)** and **(D)** APR markers, APR1 and KinA, are incorporated very early during
306 daughter cells formation and are exclusively lost in mature parasites following deletion of ERK7.
307 Western blot analysis of extracellular parasites (no or very few daughter cells present) treated with
308 IAA showed that both markers are degraded. Arrowheads indicate mother cell apex. Scale bars = 2
309 mm.

310 **Figure 3 - NHS-ester coupled with U-ExM**

311 **(A)** Maximum projection pictures of ERK7 untreated and treated parasites (non-dividing and
312 dividing) from videos 1, 2, 3 and 4. White arrowheads indicate mother cells conoid (blue
313 arrowhead: intraconoidal microtubules); yellow arrowheads highlight daughter cells conoid; red
314 arrowheads indicate deformation of the apical plasma membrane. Scale bars = 2 mm.

315

316 **Figure 4 - ERK7 depleted parasites are defective in PM integrity and microneme secretion**
317 **(A)** In both AC9 and ERK7 depletion, some parasites per vacuoles showed a defect in plasma
318 membrane integrity at the apical tip highlighted by SAG1 staining and **(B)** leaking of micronemes
319 (MIC4 staining). **(C)** Large bright field images of AC9 and EKR7 parasites treated for 48h with
320 IAA. Depleted parasites showed no defects in intracellular growth; however, parasites remained
321 trapped inside the floating host cell remnant suggesting a microneme secretion impairment. **(D)**
322 Depletion of ERK7 caused a dramatic failure in parasite to secrete microneme when stimulated with
323 ethanol (EtOH). Anti-MIC2 antibodies were used for secretion (white arrow: full length MIC2;
324 black arrow: secreted MIC2), anti-catalase (CAT) to assess parasites lysis and anti-dense granule 1
325 (GRA1) for constitutive secretion; both pellets and supernatants (SN) were analyzed. Scale bars = 2
326 µm.

327 **Figure 5 - Comparative proteomics of ERK7 and AC9 depleted parasites**
328 **(A)** and **(B)** Volcano plots showing all the proteins found in ERK7 (A) and AC9 (B) mAID
329 parasites and their differential abundance in auxin-treated parasites vs. untreated parasites. The most
330 significant changes are colored and grouped based on their known and predicted (LOPIT)
331 localization. On the left (in green) are proteins that are depleted and that majorly localize to the
332 apical complex. The proteins on the right (in magenta) are the one that are enriched and are found
333 majorly within the micronemes. **(C)** Venn diagrams showing the significant changes in ERK7 and
334 AC9 (proteins individually depleted or enriched) and the common proteins depleted or enriched in
335 both ERK7 and AC9 auxin-treated parasites. **(D)** Predicted localization of enriched and depleted
336 proteins in both ERK7 and AC9 according to hyperLOPIT.

Figure 6 – Statistically significant proteins depleted/enriched in both strains

(A) and **(B)** Heat map showing the most significant changes in both ERK7 and AC9 (auxin-treated) conditions. In green (A) are the proteins that are depleted and in magenta (B) are the proteins that are enriched. Predicted (LOPIT) localizations and previously localized proteins are also indicated. . (Hoff et al. 2001; Hu et al. 2006; de Leon et al. 2013; Tomita et al. 2013; Katris et al. 2014; Graindorge et al. 2016; Huynh & Carruthers 2016; Wall et al. 2016; Chen et al. 2017; Leung *et al.* 2017; Long *et al.* 2017a; Long et al. 2017b; Barylyuk *et al.* 2020; Tosetti *et al.* 2020)

Supplementary materials

Figure S1

(A) Mitogen-activated protein kinases (MAPKs) present in *T. gondii* and *Plasmodium* spp. **1** (Suvorova *et al.* 2015), **2** (O'Shaughnessy *et al.* 2020), **3** (Wierk et al. 2013), **4** (Dorin-Semblat et al. 2007), **5** (Fang et al. 2018), **6** (Hitz *et al.* 2020), **7** (Hu *et al.* 2020), **8** (Khan *et al.* 2005), **9** (Rangarajan *et al.* 2005), **10** (Tewari *et al.* 2005).

(B) ERK7 was C-terminally tagged with the mAID-HA construct and was tightly downregulated upon addition of auxin (IAA). **(C)** ERK7 localized at the apical cap of both mature and daughter cells. Like AC9 and AC10, ERK7 is among the earliest markers appearing during endodyogeny, before the daughter cytoskeletal basket. **(D)** ERK7 depleted parasites failed to form lysis plaques after 7 days. TIR1 represents the parental strain. **(E)** Localization of another apical cap protein (ISP1) was not majorly impacted by ERK7 degradation; nevertheless, the apical region of some parasites per vacuoles is clearly enlarged and some shows no or reduced ISP1 signal (arrowhead). Scale bars = 2 µm.

Figure S2

(A) Raw pictures and quantification of RNG1 in ERK7 inducible strain. Scale bars = 2 µm.

Figure S3

Individual stacks from videos 1, 3 and 4 highlighting the broad spectrum of NHS-ester staining for ultrastructural elements and organelles. On top left the stack number. **(A)** Ring structures observed on parasite surface (from video 1). **(B)** Apicoplast (from video 1)**.** **(C)** Rhoptry neck (from video 1). **(D)** Post-Golgi vesicles (from video 3). **(E)** Apical micronemes collar just below the conoid (from video 1). **(F)** Centrocone (white arrowhead) and centromere (yellow arrowhead) during parasite division (from video 4).

Figure S4

(A) and **(B)** Additional pictures of membrane defects in both AC9 and ERK7 and microneme leaking. **(C)** CPH1 was terminally tagged with the mAID-HA construct and was tightly downregulated upon addition of IAA by IFA. **(D)** CPH1 depleted parasites failed to form lysis plaques after 7 days. TIR1 represents the parental strain. **(E)** Depletion of CPH1 caused a moderate defect in microneme secretion when stimulated with ethanol (EtOH). Anti-MIC2 antibodies were used for secretion (white arrow: full length MIC2; black arrow: secreted MIC2) and anti-dense granule 1 (GRA1) for constitutive secretion; both pellets and supernatants (SN) were analyzed. Scale bars = 2 µm.

Figure S5

Expression profile of proteins with no "experimental localization" presented in the figure 6B. Out of 17 proteins, 7 of them (thick lines / shades of magenta) share a similar expression profile with a typical IMC protein, namely IMC1 (cyan). The 10 others, with different expression profiles, are presented with thin gray lines. Data is retrieved from the ToxoDB website (Transcriptomic data "T. gondii ME49 Cell Cycle Expression Profiles (RH)" from Behnke *et al*).

Video 1

ERK7 untreated parasite (-IAA), non-dividing cells.

Video 2

ERK7 untreated parasite (-IAA), dividing cells.

Video 3

ERK7 treated parasite (+IAA), non-dividing cells.

Video 4

ERK7 treated parasite (+IAA), dividing cells.

Material and methods

Generation of strains

T. gondii were grown in human foreskin fibroblasts (HFFs, American Type Culture Collection-CRL 1634) in Dulbecco's Modified Eagle's Medium (DMEM, Gibco) supplemented with 5% fetal calf serum (FCS), 2 mM glutamine and 25 mg/ml gentamicin. Human Foreskin Fibroblasts (HFF) were obtained from the ATCC (CRL-2088 Ref# CCD1072Sk). ERK7-mAID-HA (TGGT1_233010) was obtained by transfecting a gRNA obtained by Q5 site-directed mutagenesis kit (New England Biolabs) on the pSAG1::Cas9-U6::sgUPRT vector (Shen et al. 2014) with primer 5'-CACGCCGCATTTGTTGACTGGTTTTAGAGCTAGAAATAGC-3' and a KOD PCR obtained with F primer 5'-TTTCAGTCTGCGTCCAAGACATACAACAGCGCTAGCAAGGGCTCGGG-3' and R primer 5'-CGGCTCTTCTTTGACACAAAGCAAGAGTCTATACGACTCACTATAGGG-3' as described in (Brown et al. 2018). Depletion of ERK7-mAID-HA was obtained with 500 mM of auxin (IAA) (Brown et al. 2017). Knock-in of APR1, KinA and RNG1 were performed as previously described (Tosetti *et al.* 2020). Cloning were performed in *E. coli* XL-1 Gold chemo-competent bacteria. Freshly egressed *T. gondii* tachyzoites were transfected by electroporation and mycophenolic acid (25 mg/mL) and xanthine (50 mg/mL) (for HXGPRT cassette) or pyrimethamine (1 mg/ml) (for DHFR cassette) were employed to select resistant parasites.

Immunofluorescence assay

413 Parasites were grown in HFF cells with cover slips in 24-well plates for 24–30 hr before fixation
414 with either 4% PFA/0.05% glutaraldehyde (PFA/GA) or cold methanol and neutralized in 0.1M
415 glycine/PBS for 5 min. For SAG1 staining, parasites were permeabilized with 0.1% saponin instead
416 of Triton X-100 which was used for all other IFA. The following antibodies were used: rabbit anti-
417 IMC1 (Frenal et al. 2014), rabbit anti-HA (Sigma), mouse α-acetylated α-tubulin (6-11B-1; Santa
418 Cruz Biotechnology), mouse anti-ISP1 (Beck et al. 2010), rabbit anti-ARO (Mueller et al. 2013),
419 mouse anti-Ty, anti-MIC2 and anti-ROP2-4 (gifts from J-F Dubremetz, Montpellier), anti-tubulin
420 AA344 scFv-S11B (β-tubulin) and AA345 scFv-F2C (α-tubulin), secondary antibodies Alexa Fluor
421 405-, Alexa Fluor 488-, Alexa Fluor 594-conjugated goat a-mouse/a-rabbit. For western blot,
422 secondary peroxidase conjugated goat a-rabbit or mouse antibodies (Sigma) were used. Confocal
423 images were obtained with a Zeiss laser scanning confocal microscope (LSM700; objective
424 apochromat 63x/1.4 oil). Ultrastructure expansion microscopy (U-ExM) was performed as
425 previously described (Tosetti *et al.* 2020) and images taken with a Leica TCS SP8 STED with
426 lightning deconvolution. For intracellular conditions, the parasites were seeded on non-confluent
427 host cells in order to guarantee the good expansion of the sample. All U-ExM gels were carefully
428 measured to assure a minimum expansion ratio of 4X. The NHS-Ester staining (Thermofisher,
429 DyLight™ 488 NHS Ester) was used at 5µg/mL and incubated 1 hour in PBS. Confocal and
430 expansion images were processed with ImageJ and LAS X, respectively. Images were obtained at
431 the Bioimaging core facility of the Faculty of Medicine at University of Geneva.

432 **Plaque assay**

433 HFF were inoculated with fresh parasites and grown for 7 days with or without IAA. HFF were
434 then fixed with PAF/GA, washed once with PBS and stained with crystal violet

435 **Microneme secretion**

436 After ~48 hr of grown parasites were harvested and centrifuged at 1000g. Pellets were then washed
437 twice in intracellular buffer pre-warmed at 37˚C (5 mM NaCl, 142 mM KCl, 1 mM MgCl2, 2 mM
438 EGTA, 5.6 mM glucose and 25 mM HEPES, pH 7.2). Next, parasites were incubated at 37˚C for 15

439 min in DMEM containing 2% of ethanol (EtOH). After induction, parasite were centrifuged at 1000
440 g for 5 min at 4˚C and supernatants (SN) collected in different tubes and centrifuged at higher speed
441 (2000 g) for 5 min at 4˚C to clean from parasite debris; pellets were washed once in PBS. Pellets
442 and SNs were analyzed using anti-MIC2, anti-catalase (CAT; parasite lysis control) and anti-dense
443 granule 1 (GRA1; constitutive secretion control) antibodies by western blot.

444 **Deoxycholate extraction**

445 Freshly egressed parasites (-/+ IAA) were deposited on top of poly-L-Lysine-coated coverslips and
446 treated with 10 mM deoxycholate (20 min at room temperature). Parasites were fixed with cold
447 methanol for 8 min and immunofluorescence performed with α-acetylated α-tubulin antibody.

448 **Mass spectrometry**

449 **Sample preparation:** Parasite pellets were resuspended in 100 µl of 1 % RapiGest Surfactant
450 (Waters) in 0.1M triethylammonium bicarbonate (TEAB) and 7.5 mM Dithioerythritol (DTE).
451 Samples were heated for 5 min at 95°C. Lysis was performed by sonication (6 x 30 sec.) at 70%
452 amplitude and 0.5 pulse. Samples were kept 30 sec. on ice between each cycle of sonication.
453 Samples were centrifuged for 5 min. at 16'000 x g. Protein concentration was measured by
454 Bradford assay and 50 µg of each sample was subjected to protein digestion as follow: sample
455 volume was adjusted to 100 µl with 0.1M TEAB to obtain a final concentration of rapigest 0.1%. 2
456 µl of Dithioerythritol (DTE) 50 mM in distilled water were added and the reduction was carried out
457 at 60°C for 1h. Alkylation was performed by adding 2 µl of iodoacetamide (400 mM in distilled
458 water) during 1 hour at room temperature in the dark. Overnight digestion was performed at 37 °C
459 with 5 µl of freshly prepared trypsin (Promega; 0.2 µg/µl in TEAB 0.1M). To remove RapiGest,
460 samples were acidified with TFA, heated at 37°C for 45 min. and centrifuged 10 min. at 14'000 g.
461 Supernatants were then desalted with a C18 microspin column (Harvard Apparatus, Holliston, MA,
462 USA) according to manufacturer's instructions, completely dried under speed-vacuum and stored at
463 -20°C.

ESI-LC-MSMS: Samples were diluted in 50 µl of loading buffer (5% CH3CN, 0.1% FA) and 2 µl were injected on column. LC-ESI-MS/MS was performed on an Orbitrap Fusion Lumos Tribrid mass spectrometer (Thermo Fisher Scientific) equipped with an Easy nLC1200 liquid chromatography system (Thermo Fisher Scientific). Peptides were trapped on a Acclaim pepmap100, C18, 3µm, 75µm x 20mm nano trap-column (Thermo Fisher Scientific) and separated on a 75 µm x 500 mm, C18 ReproSil-Pur (Dr. Maisch GmBH), 1.9 µm, 100 Å, home-made column. The analytical separation was run for 180 min using a gradient of H2O/FA 99.9%/0.1% (solvent A) and CH3CN/FA 99.9%/0.1% (solvent B). The gradient was run from 5 % B to 28 % B in 160 min, then to 40% B in 20 min, then to 95%B in 10 min with a final stay of 20 min at 95 % B. Flow rate was of 250 nL/min an total run time was of 210 min. Data-dependent analysis (DDA) was performed with MS1 full scan at a resolution of 120'000 FWHM followed by as many subsequent MS2 scans on selected precursors as possible within 3 second maximum cycle time

Database search: Peak lists (MGF file format) were generated from raw data using the MS Convert conversion tool from ProteoWizard. The peaklist files were searched against the *Toxoplasma gondii GT1* database (ToxoDB, release 48, 8460 entries) combined with an in-house database of common contaminant using Mascot (Matrix Science, London, UK; version 2.5.1). Trypsin was selected as the enzyme, with one potential missed cleavage. Precursor ion tolerance was set to 10 ppm and fragment ion tolerance to 0.02 Da. Variable amino acid modifications were oxidized methionine and deaminated (NQ). Fixed amino acid modification was carbamidomethyl cysteine. The Mascot searches were validated using Scaffold 4.11.1 (Proteome Software). Peptide identifications were accepted if they could be established at greater than 91.0% probability to achieve an FDR less than 0.1% by the Scaffold Local FDR algorithm. Protein identifications were accepted if they could be

490 established at greater than 96.0% probability to achieve an FDR less than 1.0% and contained at
491 least 2 identified peptides. Protein probabilities were assigned by the Protein Prophet algorithm
492 (Nesvizhskii et al. 2003). Proteins that contained similar peptides and could not be differentiated
493 based on MS/MS analysis alone were grouped to satisfy the principles of parsimony.

494 **Comparative proteomics:** Bioinformatics analysis: For the comparative proteomics analysis, the
495 average of the three replicates (minus and plus auxin, IAA) was used to compute the false discovery
496 rate (FDR). A cutoff of 0.05 on the FDR was applied to obtain the most significant hits. For the
497 volcano plots, the log10 of the FDR (y-axis) and the log2 fold change (FC), comparing minus and
498 plus auxin treated parasites (x-axis) was computed. A cutoff of 0.5 was applied to the log2FC to
499 mark the significant changes. The plots were generated using R statistical software, and the heat
500 map with the common significant changes (depleted and enriched proteins) in both ERK7 and AC9
501 plus auxin was generated using GraphPad Prism v9. All the raw data can be found in
502 Supplementary Table S1.

503

504 **Acknowledgements**

505 We thank the Bioimaging Core Facility and the Proteomic Core Facility (University of Geneva –
506 CMU) for their excellent technical support. We thank the Brochet lab and the Guichard/Hamel lab
507 for their helpful discussion to improve the U-ExM technology. This work was supported by the
508 Swiss National Science Foundation (SNSF) 310030_185325 to DSF.

509

510 **References**

511 1. Back P.S., O'Shaughnessy W.J., Moon A.S., Dewangan P.S., Hu X., Sha J., Wohlschlegel J.A., Bradley
512 P.J. & Reese M.L. (2020) Ancient MAPK ERK7 is regulated by an unusual inhibitory scaffold required
513 for *Toxoplasma* apical complex biogenesis. Proc Natl Acad Sci U S A 117, 12164-73.
514 2. Barylyuk K., Koreny L., Ke H., Butterworth S., Crook O.M., Lassadi I., Gupta V., Tromer E., Mourier T.,
515 Stevens T.J., Breckels L.M., Pain A., Lilley K.S. & Waller R.F. (2020) A Comprehensive Subcellular
516 Atlas of the *Toxoplasma* Proteome via hyperLOPIT Provides Spatial Context for Protein Functions.
517 Cell Host Microbe 28, 752-66 e9.

518 3. Beck J.R., Rodriguez-Fernandez I.A., de Leon J.C., Huynh M.H., Carruthers V.B., Morrissette N.S. &
519 Bradley P.J. (2010) A novel family of *Toxoplasma* IMC proteins displays a hierarchical organization
520 and functions in coordinating parasite division. PLoS Pathog 6, e1001094.
521 4. Bisio H. & Soldati-Favre D. (2019) Signaling Cascades Governing Entry into and Exit from Host Cells
522 by *Toxoplasma gondii*. Annu Rev Microbiol 73, 579-99.
523 5. Brown K.M., Long S. & Sibley L.D. (2017) Plasma Membrane Association by N-Acylation Governs
524 PKG Function in *Toxoplasma gondii*. mBio 8.
525 6. Brown K.M., Long S. & Sibley L.D. (2018) Conditional Knockdown of Proteins Using Auxin-inducible
526 Degron (AID) Fusions in *Toxoplasma gondii*. Bio Protoc 8.
527 7. Chen A.L., Moon A.S., Bell H.N., Huang A.S., Vashisht A.A., Toh J.Y., Lin A.H., Nadipuram S.M., Kim
528 E.W., Choi C.P., Wohlschlegel J.A. & Bradley P.J. (2017) Novel insights into the composition and
529 function of the *Toxoplasma* IMC sutures. Cell Microbiol 19.
530 8. Damstra H.G.J., Mohar B., Eddison M., Akhmanova A., Kapitein L.C. & Tillberg P.W. (2021)
531 Visualizing cellular and tissue ultrastructure using Ten-fold Robust Expansion Microscopy (TREx).
532 bioRxiv, 2021.02.03.428837.
533 9. de Leon J.C., Scheumann N., Beatty W., Beck J.R., Tran J.Q., Yau C., Bradley P.J., Gull K., Wickstead
534 B. & Morrissette N.S. (2013) A SAS-6-like protein suggests that the *Toxoplasma* conoid complex
535 evolved from flagellar components. Eukaryot Cell 12, 1009-19.
536 10. Dorin-Semblat D., Quashie N., Halbert J., Sicard A., Doerig C., Peat E., Ranford-Cartwright L. &
537 Doerig C. (2007) Functional characterization of both MAP kinases of the human malaria parasite
538 *Plasmodium falciparum* by reverse genetics. Mol Microbiol 65, 1170-80.
539 11. Dos Santos Pacheco N., Tosetti N., Koreny L., Waller R.F. & Soldati-Favre D. (2020) Evolution,
540 Composition, Assembly, and Function of the Conoid in Apicomplexa. Trends Parasitol 36, 688-704.
541 12. Fang H., Gomes A.R., Klages N., Pino P., Maco B., Walker E.M., Zenonos Z.A., Angrisano F., Baum J.,
542 Doerig C., Baker D.A., Billker O. & Brochet M. (2018) Epistasis studies reveal redundancy among
543 calcium-dependent protein kinases in motility and invasion of malaria parasites. Nat Commun 9,
544 4248.
545 13. Francia M.E., Bhavsar S., Ting L.M., Croken M.M., Kim K., Dubremetz J.F. & Striepen B. (2020) A
546 Homolog of Structural Maintenance of Chromosome 1 Is a Persistent Centromeric Protein Which
547 Associates With Nuclear Pore Components in Toxoplasma gondii. Front Cell Infect Microbiol 10,
548 295.
549 14. Frenal K., Marq J.B., Jacot D., Polonais V. & Soldati-Favre D. (2014) Plasticity between MyoC- and
550 MyoA-glideosomes: an example of functional compensation in *Toxoplasma gondii* invasion. PLoS
551 Pathog 10, e1004504.
552 15. Graindorge A., Frenal K., Jacot D., Salamun J., Marq J.B. & Soldati-Favre D. (2016) The Conoid
553 Associated Motor MyoH Is Indispensable for *Toxoplasma gondii* Entry and Exit from Host Cells. PLoS
554 Pathog 12, e1005388.
555 16. Harding C.R., Gow M., Kang J.H., Shortt E., Manalis S.R., Meissner M. & Lourido S. (2019) Alveolar
556 proteins stabilize cortical microtubules in Toxoplasma gondii. Nat Commun 10, 401.
557 17. Hitz E., Balestra A.C., Brochet M. & Voss T.S. (2020) PfMAP-2 is essential for male gametogenesis in
558 the malaria parasite *Plasmodium falciparum*. Sci Rep 10, 11930.
559 18. Hoff E.F., Cook S.H., Sherman G.D., Harper J.M., Ferguson D.J., Dubremetz J.F. & Carruthers V.B.
560 (2001) *Toxoplasma gondii*: molecular cloning and characterization of a novel 18-kDa secretory
561 antigen, TgMIC10. Exp Parasitol 97, 77-88.
562 19. Hu K., Johnson J., Florens L., Fraunholz M., Suravajjala S., DiLullo C., Yates J., Roos D.S. & Murray
563 J.M. (2006) Cytoskeletal components of an invasion machine--the apical complex of *Toxoplasma*
564 *gondii*. PLoS Pathog 2, e13.
565 20. Hu K., Roos D.S. & Murray J.M. (2002) A novel polymer of tubulin forms the conoid of *Toxoplasma*
566 *gondii*. Journal of Cell Biology 156, 1039-50.
567 21. Hu X., O'Shaughnessy W.J., Beraki T.G. & Reese M.L. (2020) Loss of the Conserved Alveolate Kinase
568 MAPK2 Decouples *Toxoplasma* Cell Growth from Cell Division. mBio 11.
569 22. Huynh M.H. & Carruthers V.B. (2016) A *Toxoplasma gondii* Ortholog of *Plasmodium* GAMA
570 Contributes to Parasite Attachment and Cell Invasion. mSphere 1.

571 23. Kafsack B.F., Pena J.D., Coppens I., Ravindran S., Boothroyd J.C. & Carruthers V.B. (2009) Rapid
572 membrane disruption by a perforin-like protein facilitates parasite exit from host cells. Science 323,
573 530-3.
574 24. Katris N.J., van Dooren G.G., McMillan P.J., Hanssen E., Tilley L. & Waller R.F. (2014) The apical
575 complex provides a regulated gateway for secretion of invasion factors in *Toxoplasma*. PLoS Pathog
576 10, e1004074.
577 25. Khan S.M., Franke-Fayard B., Mair G.R., Lasonder E., Janse C.J., Mann M. & Waters A.P. (2005)
578 Proteome analysis of separated male and female gametocytes reveals novel sex-specific
579 *Plasmodium* biology. Cell 121, 675-87.
580 26. Lacey M.R., Brumlik M.J., Yenni R.E., Burow M.E. & Curiel T.J. (2007) *Toxoplasma gondii* expresses
581 two mitogen-activated protein kinase genes that represent distinct protozoan subfamilies. J Mol
582 Evol 64, 4-14.
583 27. Lagal V., Binder E.M., Huynh M.H., Kafsack B.F., Harris P.K., Diez R., Chen D., Cole R.N., Carruthers
584 V.B. & Kim K. (2010) *Toxoplasma gondii* protease TgSUB1 is required for cell surface processing of
585 micronemal adhesive complexes and efficient adhesion of tachyzoites. Cell Microbiol 12, 1792-808.
586 28. Leung J.M., He Y., Zhang F., Hwang Y.C., Nagayasu E., Liu J., Murray J.M. & Hu K. (2017) Stability and
587 function of a putative microtubule-organizing center in the human parasite *Toxoplasma gondii*. Mol
588 Biol Cell 28, 1361-78.
589 29. Long S., Anthony B., Drewry L.L. & Sibley L.D. (2017a) A conserved ankyrin repeat-containing
590 protein regulates conoid stability, motility and cell invasion in *Toxoplasma gondii*. Nat Commun 8,
591 2236.
592 30. Long S., Brown K.M., Drewry L.L., Anthony B., Phan I.Q.H. & Sibley L.D. (2017b) Calmodulin-like
593 proteins localized to the conoid regulate motility and cell invasion by *Toxoplasma gondii*. PLoS
594 Pathog 13, e1006379.
595 31. M'Saad O. & Bewersdorf J. (2020) Light microscopy of proteins in their ultrastructural context. Nat
596 Commun 11, 3850.
597 32. Mueller C., Klages N., Jacot D., Santos J.M., Cabrera A., Gilberger T.W., Dubremetz J.F. & Soldati-
598 Favre D. (2013) The *Toxoplasma* protein ARO mediates the apical positioning of rhoptry organelles,
599 a prerequisite for host cell invasion. Cell Host Microbe 13, 289-301.
600 33. Nesvizhskii A.I., Keller A., Kolker E. & Aebersold R. (2003) A Statistical Model for Identifying Proteins
601 by Tandem Mass Spectrometry. Anal. Chem. 75, 4646-58.
602 34. Nichols B.A., Chiappino M.L. & Pavesio C.E.N. (1994) Endocytosis at the micropore ofToxoplasma
603 gondii. Parasitology Research 80, 91-8.
604 35. O'Shaughnessy W.J., Hu X., Beraki T., McDougal M. & Reese M.L. (2020) Loss of a conserved MAPK
605 causes catastrophic failure in assembly of a specialized cilium-like structure in *Toxoplasma gondii*.
606 Mol Biol Cell 31, 881-8.
607 36. Rangarajan R., Bei A.K., Jethwaney D., Maldonado P., Dorin D., Sultan A.A. & Doerig C. (2005) A
608 mitogen-activated protein kinase regulates male gametogenesis and transmission of the malaria
609 parasite *Plasmodium berghei*. EMBO Rep 6, 464-9.
610 37. Shen B., Brown K.M., Lee T.D. & Sibley L.D. (2014) Efficient gene disruption in diverse strains of
611 *Toxoplasma gondii* using CRISPR/CAS9. mBio 5, e01114-14.
612 38. Suvorova E.S., Francia M., Striepen B. & White M.W. (2015) A novel bipartite centrosome
613 coordinates the apicomplexan cell cycle. PLoS Biol 13, e1002093.
614 39. Talevich E., Mirza A. & Kannan N. (2011) Structural and evolutionary divergence of eukaryotic
615 protein kinases in Apicomplexa. BMC Evol Biol 11, 321.
616 40. Tewari R., Dorin D., Moon R., Doerig C. & Billker O. (2005) An atypical mitogen-activated protein
617 kinase controls cytokinesis and flagellar motility during male gamete formation in a malaria
618 parasite. Mol Microbiol 58, 1253-63.
619 41. Tomita T., Bzik D.J., Ma Y.F., Fox B.A., Markillie L.M., Taylor R.C., Kim K. & Weiss L.M. (2013) The
620 *Toxoplasma gondii* cyst wall protein CST1 is critical for cyst wall integrity and promotes bradyzoite
621 persistence. PLoS Pathog 9, e1003823.
622 42. Tosetti N., Dos Santos Pacheco N., Bertiaux E., Maco B., Bournonville L., Hamel V., Guichard P. &
623 Soldati-Favre D. (2020) Essential function of the alveolin network in the subpellicular microtubules
624 and conoid assembly in *Toxoplasma gondii*. Elife 9.

625 43. Tran J.Q., de Leon J.C., Li C., Huynh M.H., Beatty W. & Morrissette N.S. (2010) RNG1 is a late marker
626 of the apical polar ring in *Toxoplasma gondii*. Cytoskeleton (Hoboken) 67, 586-98.
627 44. Wall R.J., Roques M., Katris N.J., Koreny L., Stanway R.R., Brady D., Waller R.F. & Tewari R. (2016)
628 SAS6-like protein in *Plasmodium* indicates that conoid-associated apical complex proteins persist in
629 invasive stages within the mosquito vector. Sci Rep 6, 28604.
630 45. Wierk J.K., Langbehn A., Kamper M., Richter S., Burda P.C., Heussler V.T. & Deschermeier C. (2013)
631 *Plasmodium berghei* MAPK1 displays differential and dynamic subcellular localizations during liver
632 stage development. PLoS One 8, e59755.
633 46. Wilke G., Ravindran S., Funkhouser-Jones L., Barks J., Wang Q., VanDussen K.L., Stappenbeck T.S.,
634 Kuhlenschmidt T.B., Kuhlenschmidt M.S. & Sibley L.D. (2018) Monoclonal Antibodies to Intracellular
635 Stages of Cryptosporidium parvum Define Life Cycle Progression In Vitro. mSphere 3.

636

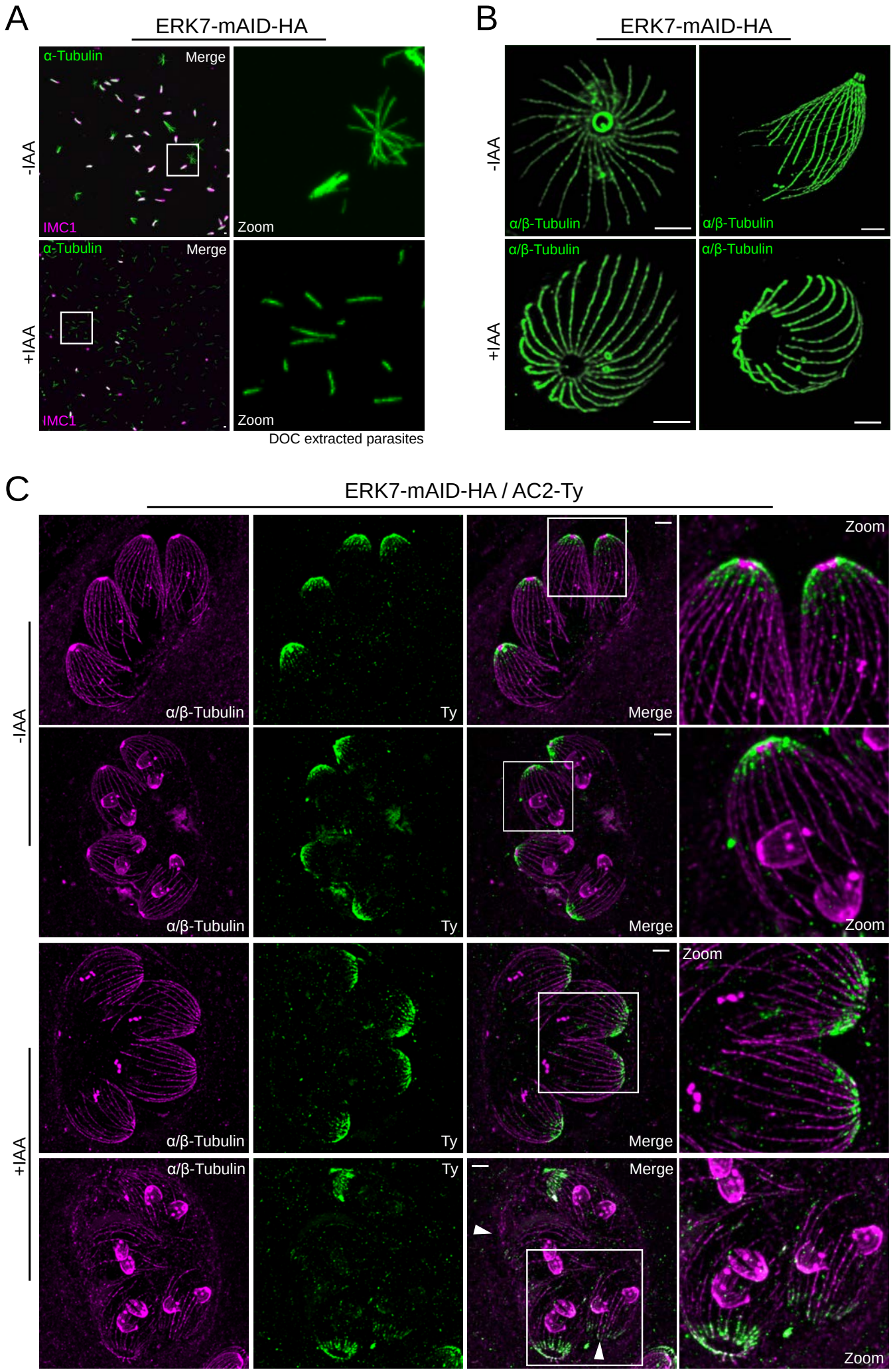
A
ERK7-mAID-HA
α-Tubulin
Merge
IMC1
Zoom
-IAA
+IAA
DOC extracted parasites
B
ERK7-mAID-HA
α/β-Tubulin
C
ERK7-mAID-HA / AC2-Ty
Ty
Merge
Zoom

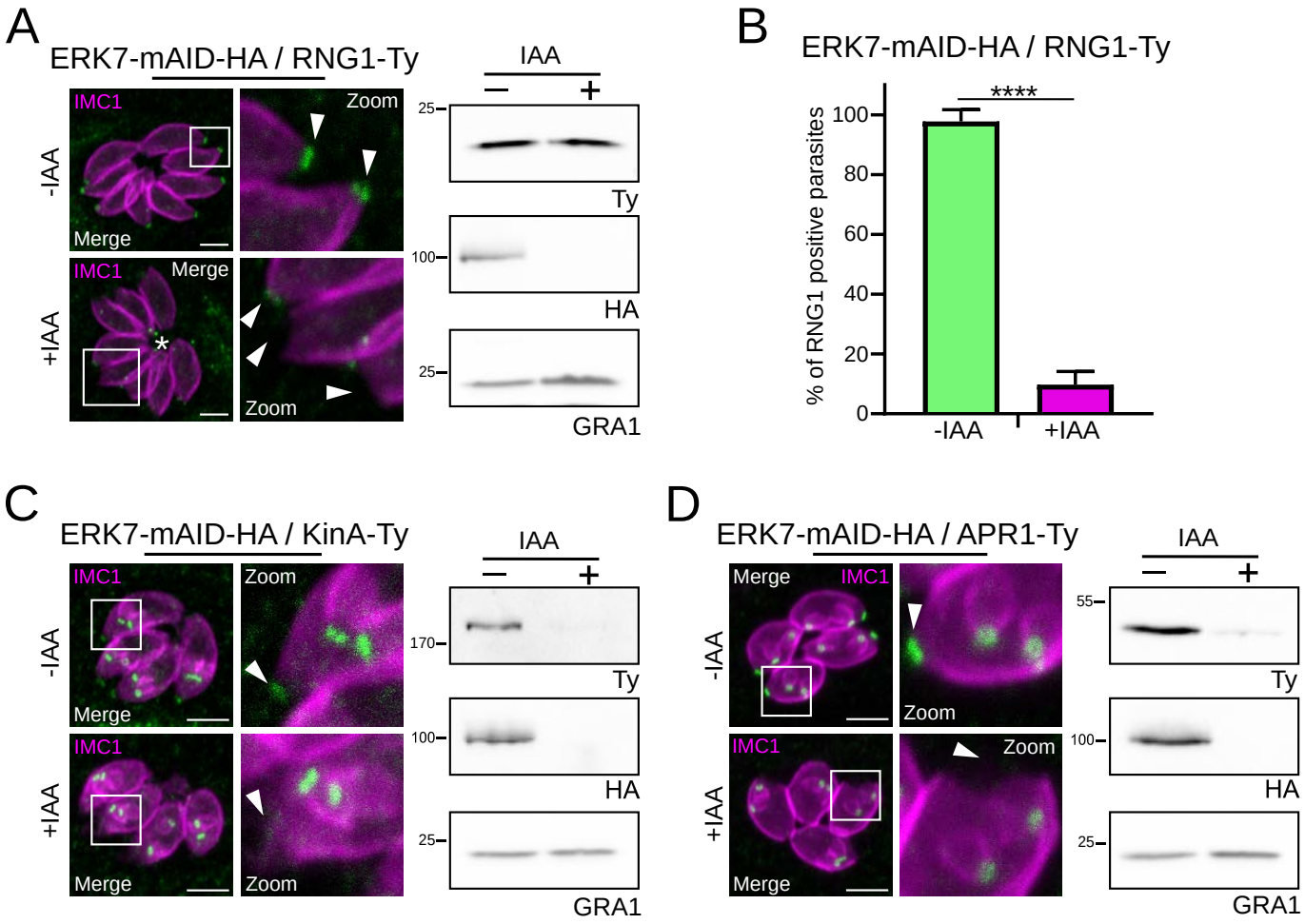
A
ERK7-mAID-HA / RNG1-Ty
IAA
–
+
-IAA
+IAA
IMC1
Merge
Zoom
25
Ty
100
HA
25
GRA1
B
ERK7-mAID-HA / RNG1-Ty
****
% of RNG1 positive parasites
100
80
60
40
20
0
-IAA
+IAA
C
ERK7-mAID-HA / KinA-Ty
170
100
25
D
ERK7-mAID-HA / APR1-Ty
55
100
25

A

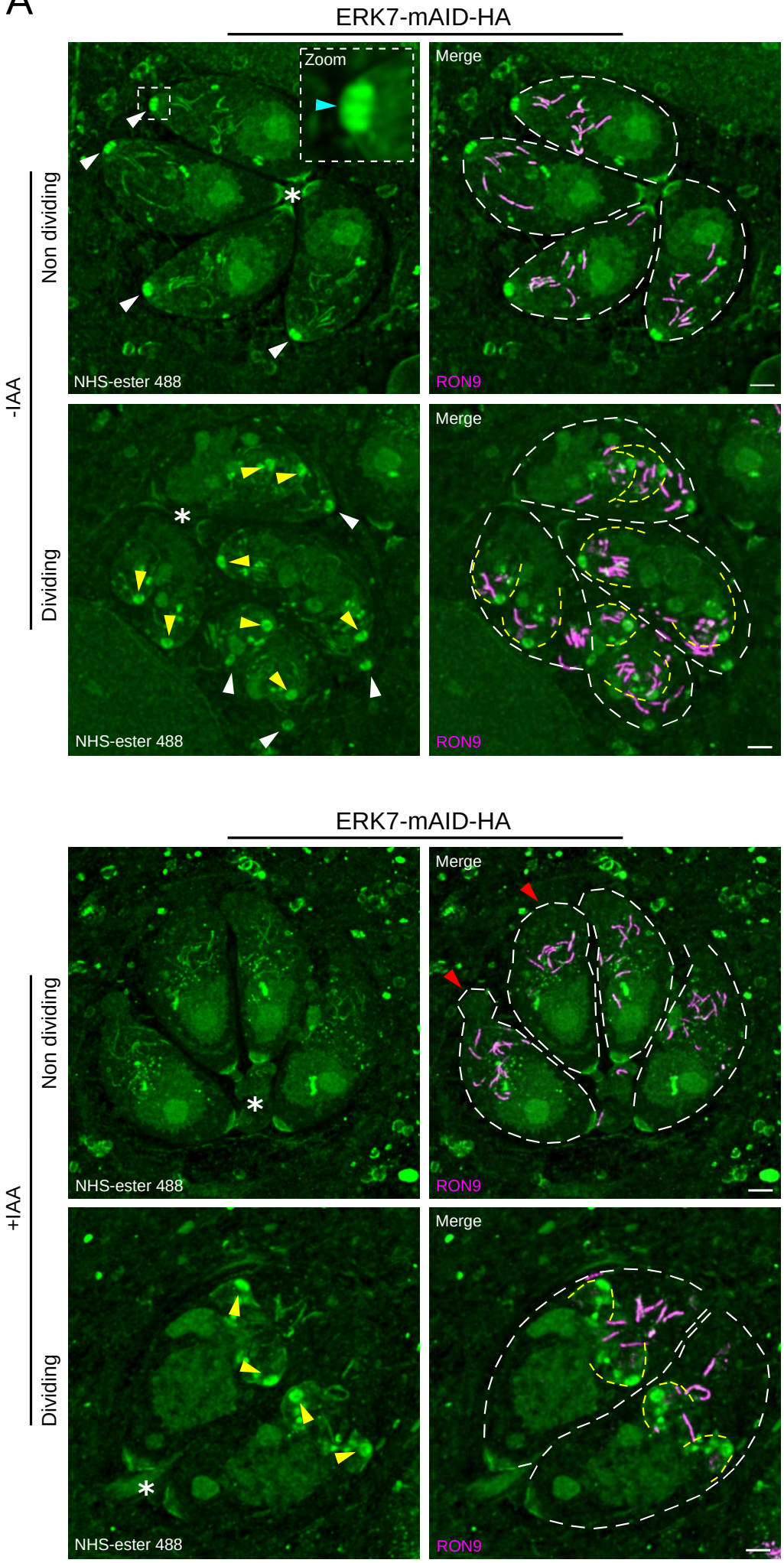
ERK7-mAID-HA
Zoom
Merge
Non dividing
-IAA
NHS-ester 488
RON9
Merge
Dividing
NHS-ester 488
RON9
ERK7-mAID-HA
Merge
Non dividing
+IAA
NHS-ester 488
RON9
Merge
Dividing
NHS-ester 488
RON9

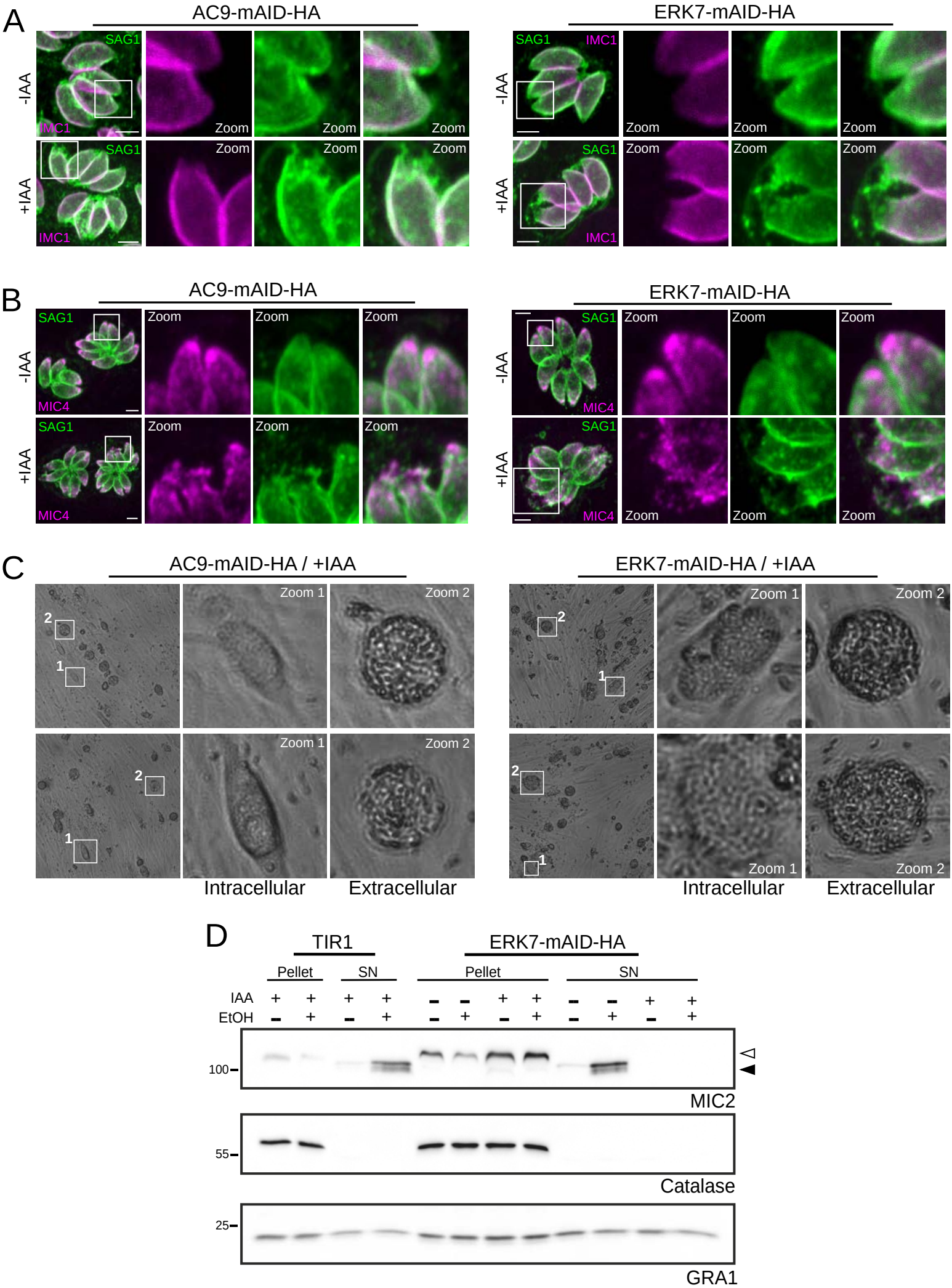
A
AC9-mAID-HA
ERK7-mAID-HA
-IAA
+IAA
SAG1
IMC1
Zoom
B
MIC4
C
AC9-mAID-HA / +IAA
ERK7-mAID-HA / +IAA
Zoom 1
Zoom 2
Intracellular
Extracellular
D
TIR1
ERK7-mAID-HA
Pellet
SN
IAA
EtOH
100
55
25
MIC2
Catalase
GRA1

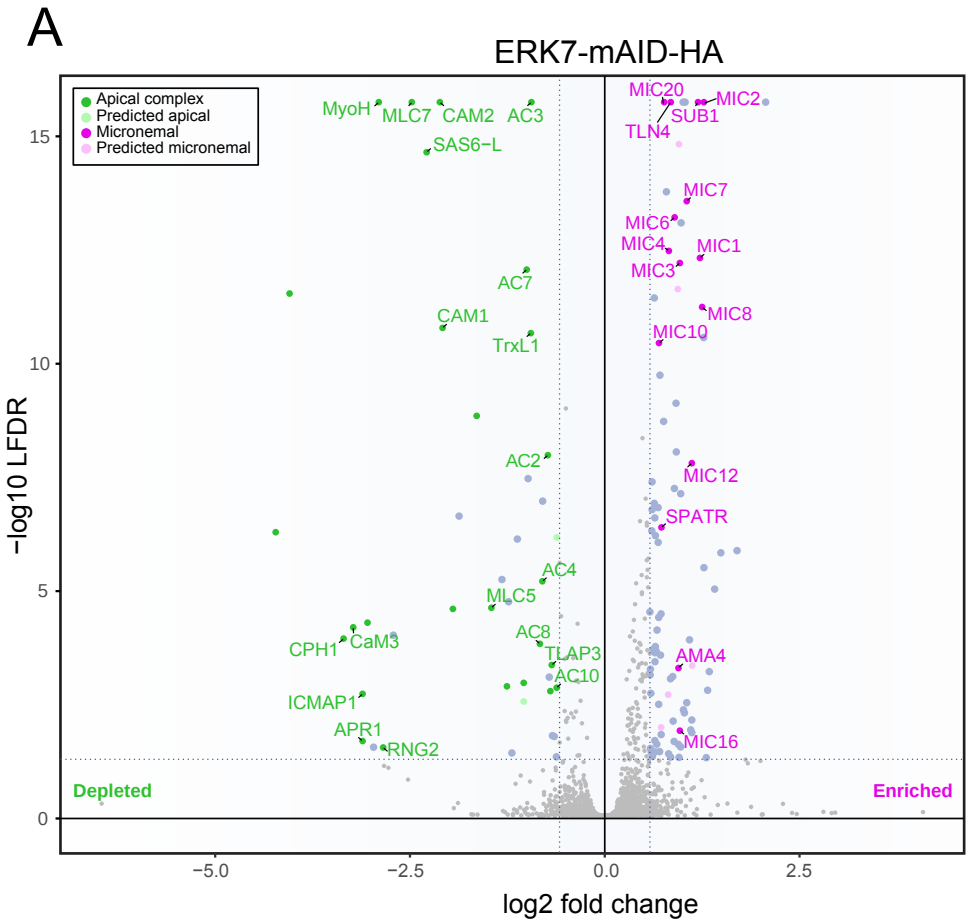
A
ERK7-mAID-HA
Apical complex
Predicted apical
Micronemal
Predicted micronemal
MyoH
MLC7
CAM2
AC3
SAS6-L
MIC20
MIC2
SUB1
TLN4
MIC7
MIC6
MIC4
MIC1
MIC3
AC7
MIC8
CAM1
MIC10
TrxL1
AC2
MIC12
SPATR
AC4
MLC5
AC8
CPH1
CaM3
TLAP3
AC10
AMA4
ICMAP1
APR1
RNG2
MIC16
Depleted
Enriched
−log10 LFDR
log2 fold change

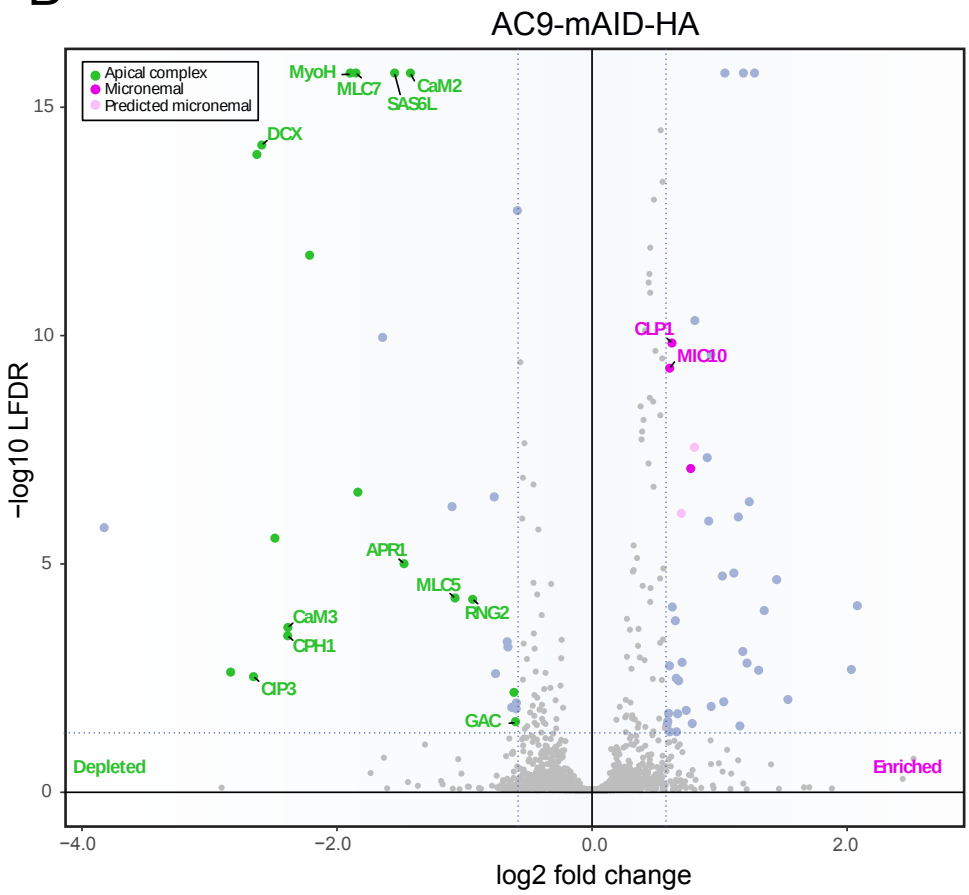
B
AC9-mAID-HA
Apical complex
Micronemal
Predicted micronemal
MyoH
MLC7
CaM2
SAS6L
DCX
GLP1
MIC10
APR1
MLC5
RNG2
CaM3
CPH1
CIP3
GAC
Depleted
Enriched
−log10 LFDR
log2 fold change

C
ERK7
Total proteins detected
3477
42 proteins
88 proteins
FDR< 0.05
DEPLETED
ENRICHED
25
17
13
65
23
18
30 proteins
41 proteins
AC9
Total proteins detected
3483

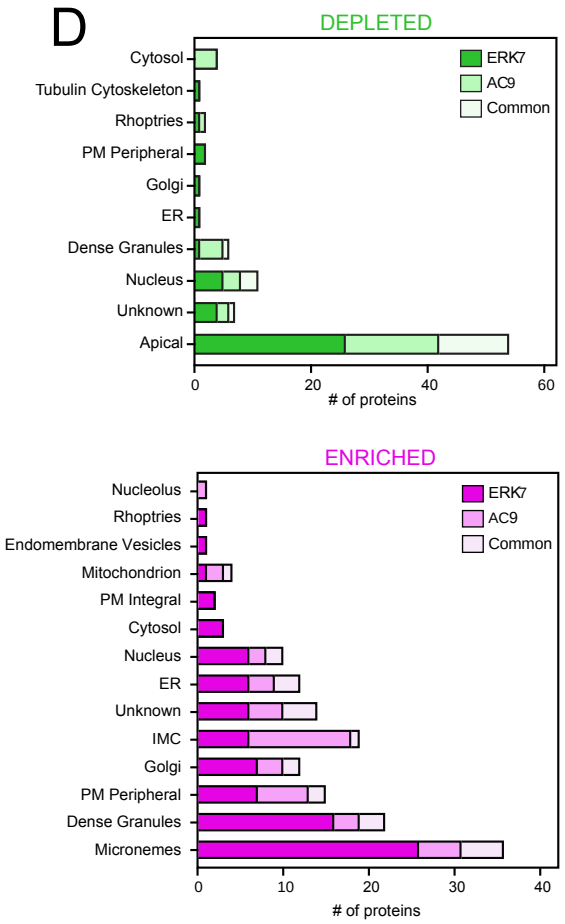
D
DEPLETED
Cytosol
Tubulin Cytoskeleton
Rhoptries
PM Peripheral
Golgi
ER
Dense Granules
Nucleus
Unknown
Apical
ERK7
AC9
Common
# of proteins
ENRICHED
Nucleolus
Rhoptries
Endomembrane Vesicles
Mitochondrion
PM Integral
Cytosol
Nucleus
ER
Unknown
IMC
Golgi
PM Peripheral
Dense Granules
Micronemes
ERK7
AC9
Common
# of proteins

A

Significant (FDR < 0.05) in both ERK7 and AC9 +IAA

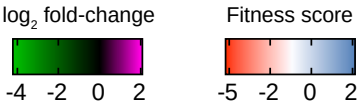

Gene name	Gene ID	DEPLETED ERK7	DEPLETED AC9	Ess CRISPR	LOPIT	Experimental localisation	Reference
-	TGGT1_222350	-4.22	-1.84	-1.31	apical 1	Conoid	(Long et al. 2017a) ; (Barylyuk et al. 2020) ; (Koreny et al. 2020)
-	TGGT1_258090	-4.05	-2.63	-1.34	apical 1	Conoid	(Long et al. 2017a) ; (Barylyuk et al. 2020) ; (Koreny et al. 2020)
CPH1	TGGT1_266630	-3.35	-2.39	-4.16	apical 1	Conoid	(Long et al. 2017a) ; (Barylyuk et al. 2020) ; (Koreny et al. 2020)
APR1	TGGT1_315510	-3.11	-1.47	-0.05	apical 1	APR	(Leung et al. 2017)
RNG2	TGGT1_244470	-2.84	-0.94	-4.21	apical 1	APR	(Tosetti et al. 2020) ; (Katris et al. 2014) ; (Koreny et al. 2020)
SAS6-L	TGGT1_301420	-2.29	-1.55	-1.62	apical 1	Conoid	(de Leon et al. 2013) ; (Wall et al. 2016) ; (Koreny et al. 2020)
CaM3	TGGT1_226040	-3.23	-2.39	-3.25	apical 2	Conoid	(Long et al. 2017b)
MyoH	TGGT1_243250	-2.90	-1.90	-3.94	apical 2	Conoid	(Graindorge et al. 2016)
MLC7	TGGT1_315780	-2.48	-1.85	-0.12	apical 2	Apical complex	(Graindorge et al. 2016)
CAM2	TGGT1_262010	-2.12	-1.42	-0.81	apical 2	Conoid	(Long et al. 2017b) ; (Hu et al. 2006)
CAM1	TGGT1_246930	-2.08	-1.22	1.09	apical 2	Conoid	(Long et al. 2017b) ; (Hu et al. 2006) ; (Graindorge et al. 2016)
MLC5	TGGT1_311260	-1.46	-1.07	-0.33	apical 2	Apical complex	(Graindorge et al. 2016)
CST1	TGGT1_264660	-0.80	-1.10	0.85	dense granules 1	Cyst wall	(Tomita et al. 2013)
-	TGGT1_246040	-2.71	-3.83	-3.29	nucleus - chromatin	-	-
-	TGGT1_315720	-1.87	-1.64	-0.39	nucleus - chromatin	-	-
-	TGGT1_254870	-1.26	-0.61	0.64	nucleus - chromatin	Apical complex	(Long et al. 2017a)
-	TGGT1_274120	-3.05	-2.49	0.64	unknown	Apical complex	(Long et al. 2017a)

B

Significant (FDR < 0.05) in both ERK7 and AC9 +IAA

Gene name	Gene ID	ENRICHED ERK7	ENRICHED AC9	Ess CRISPR	LOPIT	Experimental localisation	Reference
-	TGGT1_301480	0.84	0.60	n/a	dense granules	-	-
IMC29	TGGT1_243200	0.90	1.04	-3.95	dense granules	daughter cell IMC	(Chen et al. 2016)
-	TGGT1_250955	1.09	1.16	n/a	dense granules	-	-
-	TGGT1_238950	0.76	0.93	-3.70	ER	-	-
-	TGGT1_269340	0.89	0.79	-3.34	ER	-	-
-	TGGT1_290980	1.05	0.71	-0.62	ER	-	-
-	TGGT1_281440	0.91	0.66	-4.82	Golgi	-	-
-	TGGT1_262710	1.49	1.15	-2.62	Golgi	Golgi	(Barylyuk et al. 2020)
-	TGGT1_235690	1.12	0.61	1.12	IMC	-	-
MIC10	TGGT1_250710	0.70	0.61	2.38	micronemes	Micronemes	(Hoff et al. 2001)
-	TGGT1_221180	0.94	0.77	0.93	micronemes	Micronemes	(Barylyuk et al. 2020)
GAMA	TGGT1_243930	0.95	0.80	0.25	micronemes	Micronemes	(Huynh et al. 2016)
CLP1	TGGT1_293770	1.03	0.63	0.70	micronemes	Micronemes	ToxoDB comment
-	TGGT1_249300	1.12	0.70	2.16	micronemes	-	-
-	TGGT1_248950	0.82	0.59	-3.72	mitochondrion - membranes	-	-
-	TGGT1_320080	0.89	0.81	-0.52	nucleus - chromatin	-	-
-	TGGT1_203820	2.07	0.91	1.39	nucleus - chromatin	-	-
-	TGGT1_222370	1.70	1.31	-0.07	PM - peripheral 1	-	-
-	TGGT1_220900	1.27	0.74	-3.42	PM - peripheral 2	-	-
-	TGGT1_294640	0.68	1.19	-4.79	unknown	-	-
-	TGGT1_310220	0.87	0.90	-1.36	unknown	-	-
-	TGGT1_294610	1.27	1.27	-0.98	unknown	-	-
-	TGGT1_282070	1.34	1.18	-2.70	unknown	-	-